The current issue and full text archive of this journal is available on Emerald Insight at:
https://www.emerald.com/insight/0961-5539.htm

Received 10 April 2022
Revised 22 August 2022
28 September 2022
12 January 2023
Accepted 13 January 2023

Effects of coflow-jet active flow control on airfoil stall

Shima Yazdani and Erfan Salimipour
Department of Mechanical Engineering, Quchan University of Technology, Quchan, Iran

Ayoob Salimipour
Department of Mathematics, Quchan University of Technology, Quchan, Iran, and

Mikhail A. Sheremet and Mohammad Ghalambaz
Laboratory on Convective Heat and Mass Transfer, Tomsk State University, Tomsk, Russian Federation

Abstract

Purpose – Active flow control on the NACA 0024 airfoil defined as suction-injection jet at the chord-based Reynolds number of $1.5 \times 1e + 5$ is studied.

Design/methodology/approach – The three-dimensional incompressible unsteady Reynolds-averaged Navier–Stokes equations with the SST k-ω turbulence model are used to study the effects of coflow-jet (CFJ) on the dynamic and static stall phenomena. CFJ implementation is conducted with several momentum coefficients to investigate their turnover. Furthermore, the current work intends to analyze the CFJ performance by varying the Reynolds number and jet momentum coefficient and comparing all states to the baseline airfoil, which has not been studied in prior research investigations.

Findings – It is observed that at the momentum coefficient ($C\mu$) of 0.06, the lift coefficients at low attack angles (up to $a = 15$) dramatically increase. Furthermore, the dynamic stall at the given Reynolds number and with the lowered frequency of 0.15 is explored. In the instance of $C\mu = 0.07$, the lift coefficient curve does not show a noticeable stall feature compared to $C\mu = 0.05$, suggesting that a more powerful stronger jet can entirely control the dynamic stall.

Originality/value – Furthermore, the current work intends to analyze the CFJ performance by varying the jet momentum coefficient and comparing all states to the baseline airfoil, which has not been studied in prior research investigations.

Keywords Active flow control, Coflow-jet, Momentum coefficient, Stall

Paper type Research paper

1. Introduction

Wind turbines convert the kinetic energy of the wind into electrical energy and are categorized into two types: vertical axis and horizontal axis. Generally, although horizontal-axis wind turbines (HAWT) are popular all around the world, they cannot be used in municipal areas, damage the environment and need a high initial cost. Wind energy is considered as one the cheapest and most available renewable energy resources. However,

Data availability statement: The data that support the findings of this study are available from the corresponding author upon reasonable request.
This research of Mohammad Ghalambaz and Mikhail Sheremet was supported by the Tomsk State University Development Programme (Priority-2030). This work is based on the preprint with DOI: 10.21203/rs.3.rs-672095/v3.

International Journal of Numerical Methods for Heat & Fluid Flow
Vol. 33 No. 6, 2023
pp. 2278-2294
© Emerald Publishing Limited
0961-5539
DOI 10.1108/HFF-04-2022-0219

Downloaded from http://www.emerald.com/hff/article-pdf/33/6/2278/1441048/hff-04-2022-0219.pdf by Giresun Universitesi user on 17 August 2025

due to different problems of HAWTs, wind turbines are not widely used. Thus, vertical-axis wind turbines (VAWT) take on paramount importance (Saqib Hameed and Kamran Afaq, 2013). The most important superiority of this type of wind turbine is that they do not need to be adjusted relative to the wind direction. Regarding that the axis is vertical, the gearbox and generator can be installed near the ground, leading to maintenance and repair of these pieces of equipment. As the blade tip is closer to the rotating axis in VAWTs, in comparison to HAWTs, they make lower noise. Furthermore, due to their smaller size, the peripheral collisions are reduced.

NACA airfoils are designed for aircraft and wind turbines. Investigating airfoil characteristics, particularly in incompressible low-Reynolds flows, and changes in the aerodynamic performance of airfoils due to the amount of the Reynolds number is of paramount importance. Several investigations were conducted to study the performance of airfoils in the low Reynolds number region (Yarusevych *et al.*, 2006b; Lissaman, 1983; Mueller and DeLaurier, 2003). Some studies indicated that serious aerodynamic problems might occur for below Reynolds number of about 500,000 (Yarusevych *et al.*, 2006a; Srinath and Mittal, 2009; Salimipour, 2019a). The flow tendency through the airfoil's suction surface is to be separated in this Reynolds number range. On the other hand, the reverse pressure gradient that occurs in low Reynolds number airfoils causes the flow separation (Gim and Lee, 2013). As the angle of attack increases, the vertical velocity and, consequently, the lift coefficient are escalated. Furthermore, the drag coefficient is also enhanced, as the vertical velocity depends on the air resistance. This trend continues up to a specific angle called the stall angle. When stall happens, devastating effects on aerodynamic performance occur; the lift coefficient dramatically decreases while the drag coefficient increases (Salimipour and Yazdani, 2020; Abbasi and Yazdani, 2019). In other words, stall angle is a point beyond which the lift-to-drag ratio starts declining with angle of attack. Thus, applying methods to control the stall phenomenon and the separation flow are important.

The airfoil aerodynamic performance can be enhanced with the adequate energy and momentum transported to the boundary layer using flow control methods to reach desired aerodynamic goals, including delaying the transition, delaying the separation and improving the aerodynamic efficiency. Many successful strategies have been developed (Velasco *et al.*, 2017; Salimipour and Salimipour, 2019; Salimipour *et al.*, 2021) to regulate flow separation and avoid the stall effects. In low Reynolds number aerodynamics, changing the shape of the airfoil is often used to regulate separation and enhance the lift coefficient. Coflow-jet (CFJ) is one of the active flow control approaches. The airfoil's suction surface features two slots in this technique: an injection slot near the leading edge and a suction slot near the trailing edge. In this flow control no mass adds to the system. Suction and injection in the airfoil surface, especially at high angles of attack, along with resistance to the reverse pressure gradient, connects the main flow and boosts boundary-layer velocity. Zha *et al.* (2006) in wind tunnel investigated the effects of injection slot size on the NACA 0025 at Reynolds number $Re = 3.8 \times 10^5$. Their research revealed that although a smaller injection slot size airfoil is better for boosting lift, a wider slot minimizes drag. Zha *et al.* (2007) studied the influence of the suction slot on efficiency numerically. For this purpose, two airfoils with the same injection slot (0.65% c) were studied with the suction slot equaled to 1.96% c and the other without the suction slot. This study showed that the airfoil with the suction slot had better aerodynamic performances. For both airfoils compared to the baseline airfoil, the lift coefficient was increased and the angle of attack was delayed.

The airfoil without a suction slot, the stall occurred at 39° and the other until 43° the stall did not happen. Zha and Gao (2006) experimentally performed the effects of the CFJ on the NACA 0025 at $Re = 3.8 \times 10^5$. They looked at various pressure ratios and found that the lift

Downloaded from http://www.emerald.com/hff/article-pdf/33/6/2278/1441048/hff-04-2022-0219.pdf by Giresun Universitesi user on 17 August 2025

coefficient rose by 220% compared to the baseline in the jet case. They also numerically performed their experimental results, and there was a good agreement between the data for the lift coefficient. However, the angle of attack of the stall was forecasted in numerical results three degrees more than experiments. The effects of adjusting the injection slot size on the lift coefficient, stall angle and drag coefficient were explored experimentally by Wells *et al.* (2006). Their findings revealed that an airfoil with a smaller injection slot would need less energy to attain the same lift coefficient as one with a bigger injection slot. Chng *et al.* (2009) experimentally investigated the jet concept's performance on a Clark-Y airfoil. Furthermore, they compared the aerodynamic performance of the synchronous suction and injection, pure injection and pure suction. Their findings demonstrated that the simultaneous suction and injection mechanism are more effective than pure injection and pure suction.

Abinov *et al.* (2016), using ANSYS Fluent software, compared the performance of the NACA 6409 baseline airfoil and three jet airfoils with different injection and suction slot locations. The influence of jet on the S809 airfoil was numerically examined by Xu *et al.* (2015) at three jet momentum coefficient values. According to their findings, the jet greatly reduces the drag coefficient and positively influences lift and stall margin. Ethiraj (2017) examined the impact of jet mathematically, and obtained results for a 12° angle of the attack suggest a 25%–30% decrease in drag and a 10%–20% increase in lift coefficient. Siddanathi (2016) used a jet on NACA 652–415 airfoil to investigate this active flow control on increasing the lift. Lefebvre and Zha (2013) numerically studied the effect of jet flow control on a pitching airfoil at the Reynolds number of 3.93×10^6 and reduced frequency between 0.05 and 0.2. Moreover, Xu *et al.* (2016) simulated the dynamic stall phenomenon for a wind turbine blade using the jet. Khoshnevis *et al.* (2020) examined the effects of jets on symmetric NACA airfoils in transitional flow, considering thickness variation. In another investigation, they analyzed the influence of this flow control on NACA 0025 at different Reynolds numbers (Khoshnevis *et al.*, 2020). Some interesting results on this topic can be found in Gleize *et al.* (2022), Nived *et al.* (2022).

In the present paper, active flow control on the NACA 0024 airfoil defined as suction-injection jet at the chord-based Reynolds number of 1.5×10^5 is studied. The three-dimensional incompressible unsteady Reynolds-Averaged Navier–Stokes equations with the SST k-ω turbulence model are used to study the effects of CFJ on the dynamic and static stall phenomena. CFJ implementation is conducted with several momentum coefficients to investigate their turnover. Furthermore, the current work intends to analyze the CFJ performance by varying the jet momentum coefficient and comparing all states to the baseline airfoil, which has not been studied in prior research investigations. The work is based on the preprint (Yazdani *et al.*, 2022).

2. Model description

The CFJ is constructed at the suction surface of the baseline NACA 0024 airfoil to produce a jet tangential to the main flow; the heights of an injection slot and a suction slot are considered 0.006 and 0.019 times the chord length, respectively. The suction and injection slots are located at distances of 0.83 and 0.07 times the chord length from the leading edge. Based on the considered geometry, various meshing strategies can be used where a "C" grid is chosen to solve the flow field. Figure 1 shows a close-up view of this grid together with the situation of the CFJ on the airfoil. The nodes have an adequate perpendicular to one another, as can be shown. A width equal to the chord length is considered in the z direction, as shown in Figure 1.

Downloaded from http://www.emerald.com/hff/article-pdf/33/6/2278/1441048/hff-04-2022-0219.pdf by Giresun Universitesi user on 17 August 2025

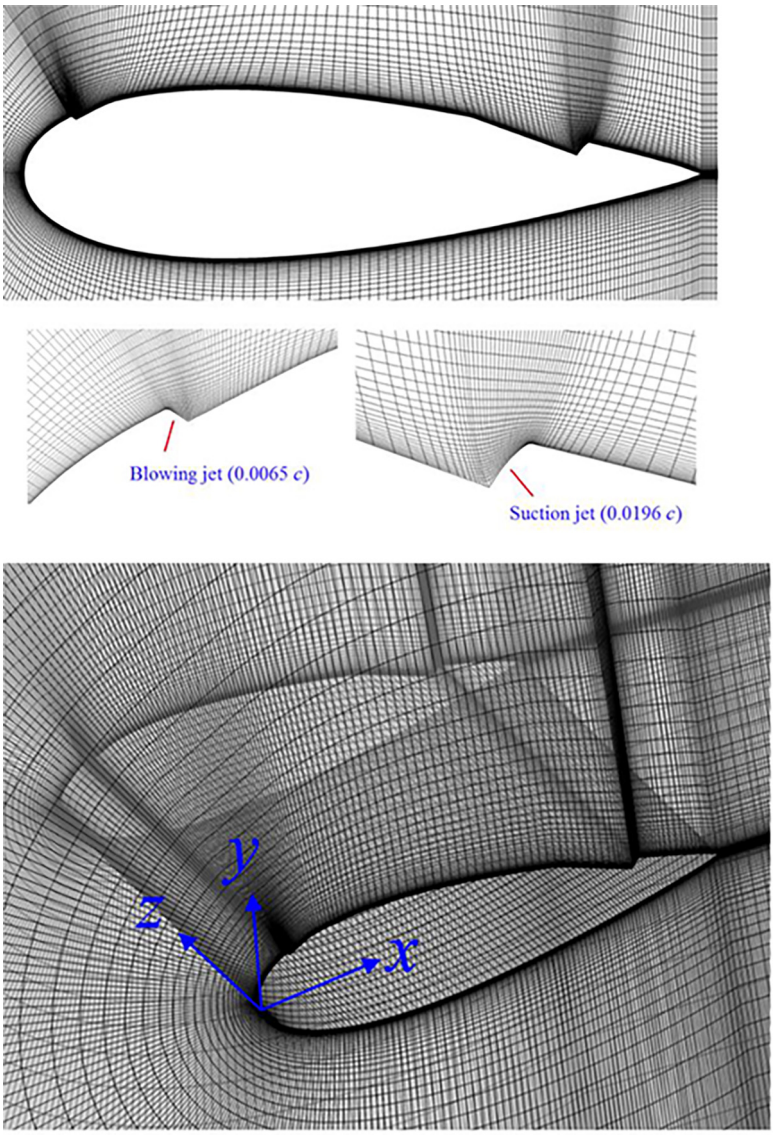

Figure 1.
The grid used in flow computations and situation of the CFJ on the airfoil

Figure 2 shows the solution domain and boundary conditions. The velocity inlet boundary includes a constant value of U_∞ for the horizontal velocity component, zero for the vertical velocity component and a zero normal gradient for the pressure (Ghalambaz *et al.*, 2020). On the pressure outlet boundary, a fixed value of p_∞ is applied for the pressure and the normal gradient of the velocities is assigned to zero. On the solid wall, a no-slip boundary condition is considered. The periodic boundary condition is used for the lateral boundaries.

Downloaded from http://www.emerald.com/hff/article-pdf/33/6/2278/1441048/hff-04-2022-0219.pdf by Giresun Universitesi user on 17 August 2025

3. Mathematical and numerical formulation

The integral formulations of the Reynolds-averaged Navier–Stokes equations, which include continuity and momentum, are as follows (Salimipour, 2019b):

$$\oint_{\partial\Omega} \rho V dS = 0 \tag{1}$$

$$\frac{\partial}{\partial t}\int_{\Omega} \overline{W} d\Omega + \oint_{\partial\Omega} \overline{J} dS = 0 \tag{2}$$

where ρ denotes the density, Ω is a volume surrounded by the control surface $\partial\Omega$, V is the velocity perpendicular to the surface element dS, $\overline{W}$ represents the conservative variables vector, and $\overline{J}$ consists of the convective and diffusive fluxes which can be written as follows (Salimipour, 2019a; Kalkote *et al.*, 2020):

$$\overline{W} = \begin{bmatrix} \rho u \\ \rho v \end{bmatrix}, \quad \overline{J} = \begin{bmatrix} \rho u V + n_x p - (\mu + \mu_t)\left(n_x \dfrac{\partial u}{\partial x} + n_y \dfrac{\partial u}{\partial y}\right) \\ \rho v V + n_y p - (\mu + \mu_t)\left(n_x \dfrac{\partial v}{\partial x} + n_y \dfrac{\partial v}{\partial y}\right) \end{bmatrix} \tag{3}$$

$$V \equiv \overline{v} \cdot \overline{n} = n_x u + n_y v \tag{4}$$

where μ and μ_t denote the laminar and turbulent viscosity, respectively. The flow equations (1) and (2) are solved by a pressure-based method proposed by Rajagopalan and Lestari (2016). The momentum equation is discretized with the second-order precision in time and space (Stone, 1968). To simulate the turbulent viscosity (μ_t), the SST k-ω turbulence model is used. The flow variables are normalized as expressed in (Hashem Zadeh *et al.*, 2020). The flow parameters required, such as velocity and pressure components, streamlines and drag and lift coefficients, could be obtained by numerically solving the previously given equations. The jet momentum coefficient C_μ is a parameter that is used to determine the strength of the jet. It is as follows (Bak Khoshnevis *et al.*, 2020):

$$C_\mu = \frac{\dot{m} U_j}{0.5 \rho_\infty U_\infty^2 c} \tag{5}$$

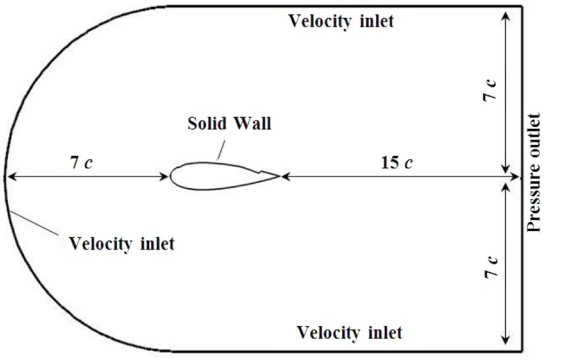

Figure 2.
Boundary conditions around the NACA 0024 airfoil

Downloaded from http://www.emerald.com/hff/article-pdf/33/6/2278/1441048/hff-04-2022-0219.pdf by Giresun Universitesi user on 17 August 2025

where U_j and $\dot{m}$ denote the velocity and mass flow of injection; U_∞ and ρ_∞ are the free stream velocity and density; and c is the airfoil chord length. For cases with a CFJ on, the overall aerodynamic force is estimated according to the analysis in Zha *et al.* (2007), Xu *et al.* (2015). The following is an expression for the overall lift and drag coefficients:

$$C_l = C_{l,pressure} + C_{l,stress} + C_{l,jet} \tag{6}$$

$$C_d = C_{d,pressure} + C_{d,stress} + C_{d,jet} \tag{7}$$

where subscripts *pressure*, *stress* and *jet* indicate the pressure force, frictional force and jet mass flow thrust, respectively. $C_l = C_{l,pressure+stress}$ and $C_d = C_{d,pressure+stress}$ be computed using the solver's standard integral approach, while $C_{l,jet}$ and $C_{d,jet}$ are achieved using relations as follows:

$$C_{l,jet} = \frac{\dot{m}_j\left(\overline{V}_{j1} - \overline{V}_{j2}\right)\overline{J}}{0.5\rho_\infty U_\infty^2 c} \tag{8}$$

$$C_{d,jet} = \frac{\dot{m}_j\left(\overline{V}_{j1} - \overline{V}_{j2}\right)\overline{i}}{0.5\rho_\infty U_\infty^2 c} \tag{9}$$

where $(\overline{i},\overline{J})$ is the unit vector indicating the lift and drag direction and $\overline{V}_{j1}$, $\overline{V}_{j2}$ are velocity vectors of the jet at injection and suction slots, respectively.

The pitching motion of the airfoil for dynamic stall analysis is described by the following equation:

$$\alpha(t) = 10^\circ + 10^\circ \cdot sin(2k\tau) \tag{10}$$

where $k = \frac{\omega c}{(2U_\infty)}$ is the reduced frequency and $\tau = \frac{tU_\infty}{c}$ denotes the non-dimensional time. For quantifying the improvement of results from CFJ to enhance lift and decrease drag coefficients for the dynamic stall study, the differences in the area under C_l and C_d curves between control cases and the baseline airfoil are calculated. This is accomplished as follows (where q is either lift or drag):

$$\Delta A_{C_q} = \frac{\int_0^{2\pi}\left(C_q^{baseline} - C_q^{CFJ}\right)d\phi}{\int_0^{2\pi} C_q^{baseline}\,d\phi} \tag{11}$$

where φ denotes the phase angle of the pitching motion in radians.

4. Results and discussion

4.1 Grid resolution study

The grid convergence index (GCI) is applied to evaluate the uncertainty caused by the grid spacing. For three mesh resolutions of 1: coarse, 2: medium and 3: fine, the GCI formulation based on the Richardson's extrapolation theory can be written as follows (Lee *et al.*, 2020):

$$GCI_{i,i+1} = F_S\frac{|\varepsilon_{i,i+1}|}{r^p - 1}, \quad i = 1,\ 2,\ 3 \tag{12}$$

Downloaded from http://www.emerald.com/hff/article-pdf/33/6/2278/1441048/hff-04-2022-0219.pdf by Giresun Universitesi user on 17 August 2025

$$\varepsilon_{i,i+1} = \frac{f_i - f_{i+1}}{f_{i+1}} \tag{13}$$

$$p = \frac{\ln\left|\frac{(f_1 - f_2)}{(f_2 - f_3)}\right|}{\ln(r)} \tag{14}$$

where F_S, ε, r, p and f are the safety factor, relative error, ratio of grid refinement, accuracy order and solution value, respectively. For three meshes, F_S = 1.25 (Lee *et al.*, 2020). The lower value of the GCI is the lower the grid sensitivity.

In the present study, three meshes with 1: 640,000, 2: 900,000 and 3: 1,260,000 points on three directions with a constant r = *1*.4 are generated and 30 points are considered at z direction to capture the three-dimensional effects. Two solution values of C_l and C_d are examined for the GCI study at $\alpha = 15^{\circ}$, $Re = 1.5 \times 10^5$ and C_μ = 0.13. Table 1 presents the GCI calculations for the above-mentioned meshes. Due to the low percentage of the GCI_{23}, the medium mesh is used for the computations.

The y^+ dimensionless parameter is an important parameter for determining the grid quality used to solve turbulent flow problems. Figure 3 depicts the wall y^+ distribution of the CFJ airfoil at C_μ = 0.07 and $\alpha = 15^{\circ}$. As can be seen, the maximum value of y^+ reaches about 1.5.

4.2 Code validation research

It is vital to assess the flow solver validity before using the developed code and validating its correctness. Experimental data obtained by Ziadé *et al.* (2018) is used to assess the solver

Table 1.
GCI Calculations for lift and drag coefficients at $\alpha = 15^{\circ}$, $re = 1.5 \times 10^5$ and C_μ = 0.13

	f_1 (coarse)	f_2 (medium)	f_3 (fine)	GCI_{12} (%)	GCI_{23} (%)
C_l	2.12	2.24	2.25	0.61	0.05
C_d	0.28	0.22	0.214	6.81	0.7

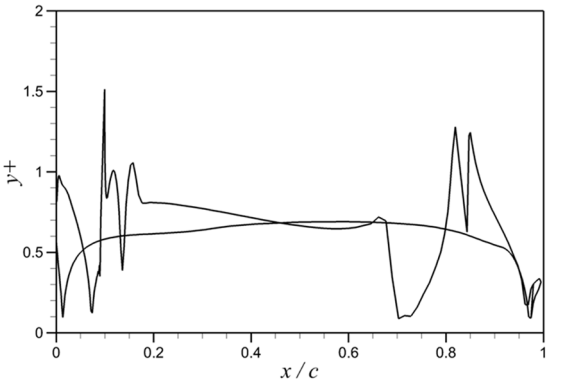

Figure 3.
$y+$ distribution of the bladed airfoil's surface

Downloaded from http://www.emerald.com/hff/article-pdf/33/6/2278/1441048/hff-04-2022-0219.pdf by Giresun Universitesi user on 17 August 2025

capabilities for the configuration of the NACA 0025 at $Re = 10^5$. Figure 4 compares the pressure coefficient distribution of the current solution and the experimental data. The prognostications are in nearby conjunction with the experiment.

At the Reynolds number of 5×10^4 and $\alpha = 9.25°$, the skin friction coefficient of the NACA 0012 airfoil computed by the present solver is compared with the direct numerical simulation data obtained by Rodríguez *et al.* (2013). As shown in Figure 5, an acceptable correspondence with the DNS data is observed for the skin friction coefficient on the upper surface of the airfoil.

The next case investigates the solver's ability to simulate the flow past pitching airfoil along with dynamic stall. Figure 6 compares the lift and drag coefficients as a function of attack angle with the experimental results from Lee and Gerontakos (2004) at $k = 0.15$ and $Re = 1.35 \times 10^5$. The present results seem to be in a good correspondence with the experimental data except for predicting the lift coefficient at $\alpha = 20°$ and also for $17° < \alpha < 19°$ in pitch down motion.

4.3 Effect of momentum coefficient of coflow-jet on static stall at re = 1.5 × 10^5

In this study, several momentum coefficients (C_μ) for the angles of attack in the range of 0°–30° at $Re = 1.5 \times 10^5$ on the NACA 0024 airfoil are investigated to understand which momentum

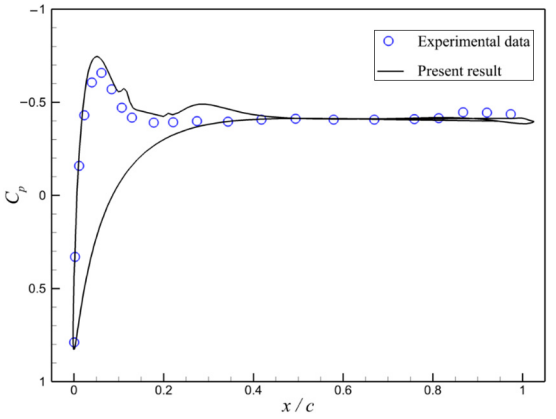

Figure 4. Comparison of pressure coefficient distribution of NACA 0025 airfoil between present result and experimental data (Ziadé *et al.*, 2018) at $Re = 10^5$ and $\alpha = 12°$

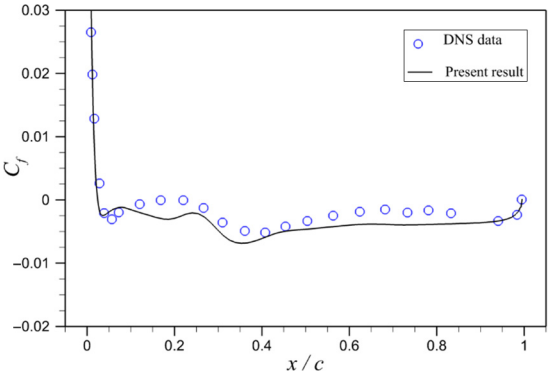

Figure 5. Comparison of skin friction coefficient of NACA 0012 airfoil between present result and DNS data (Rodríguez *et al.*, 2013) at $Re = 5 \times 10^4$ and $\alpha = 9.25°$

Downloaded from http://www.emerald.com/hff/article-pdf/33/6/2278/1441048/hff-04-2022-0219.pdf by Giresun Universitesi user on 17 August 2025

coefficient has an agreeable act at each attack angle. Figure 7 shows the pressure coefficients streamtraces and contours for the baseline geometry at the angles of attack $\alpha = 5°$, 10° and 15°. The growth of the vortices can be seen for $\alpha \geq 5°$. The entanglement of the streamtraces in Figure 7(c) indicates the presence of three-dimensional effects that arise from the third dimension (z-direction) disturbances.

Figure 8 shows the streamtraces around the CFJ airfoil with $C_\mu = 0.05$ at $\alpha = 15°$. By applying the CFJ, the vortices on the airfoil are removed. The CFJ injects momentum into the boundary layer, resisting the flow separation because of the adverse pressure gradient.

Figure 9 shows the pressure coefficient distributions of the baseline and CFJ airfoils at $\alpha = 15°$ and $C_\mu = 0.05$, 0.09 and 0.13. The spikes in the plots are due to the jet inlet and outlets. The comparisons demonstrate that the suction peak around the leading edge of the CFJ airfoils is much greater than that of the baseline airfoil. This effect causes the airfoil's lift to rise while decreasing its pressure drag. The pressure coefficient has a maximum absolute value of 7 at $C_\mu = 0.13$, whereas the baseline airfoil has a value of 1.9. The temporal fluctuations of the lift coefficients for baseline and CFJ airfoils with varying momentum coefficients $\alpha = 15°$ are shown in Figure 10.

It can be seen that all the curves finally become unchanged over time, and thus, the flow at this angle of attack has been steady. Furthermore, the baseline airfoil curve trend indicates that the stall occurs at this angle of attack, unlike the other curves.

The lift to drag ratio is an essential statistic for aircraft aerodynamic performance. Figure 11 depicts the lift to drag coefficient curves for various momentum coefficients with respect to the angle of attack. The CFJ airfoils, compared to the baseline airfoil, have a dramatic gain in the lift to drag coefficients and cause the stall to occur at the higher angles of attack maintained with higher values of C_μ. As observed, increasing the momentum coefficient increases the stall angles and maximum lift to drag coefficients for all CFJ airfoils.

The lift to drag coefficient diagram shows that for the CFJ airfoil with $C_\mu = 0.05$, there is a significant increase for the C_l/C_d, and the stall angle is delayed compared to the baseline airfoil. At $C_\mu = 0.06$ and $\alpha \leq 15°$, the highest C_l/C_d is observed. As the angle of attack increases from $\alpha = 20°$ to 30°, the C_l/C_d decreases. At $C_\mu = 0.13$ and $\alpha \leq 10°$, the use of CFJ is not optimum because of the drag increment, while for $\alpha \geq 15°$, a significant C_l/C_d is obtained because of the significant lift generation. For the other angles, the maximum C_l/C_d is distinct at each angle of attack. The baseline airfoil result shows the stall occurrence around $\alpha = 10°$, whereas for the CFJ airfoils results with $C_\mu = 0.05$–0.07, the stall occurs at $\alpha = 15°$. With further increase in the momentum coefficients, the stall angles increase, and at $C_\mu = 0.13$, the stall does not occur up to

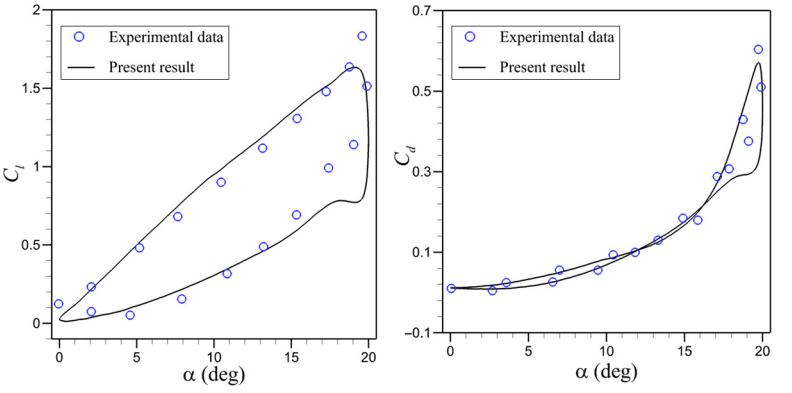

Figure 6.
Comparison of the lift and drag coefficients of NACA 0012 airfoil with the experimental data (Lee and Gerontakos, 2004) at $k = 0.15$, $\alpha_m = 10°$, $\alpha_0 = 10°$ and $Re = 1.35 \times 10^5$

Downloaded from http://www.emerald.com/hff/article-pdf/33/6/2278/1441048/hff-04-2022-0219.pdf by Giresun Universitesi user on 17 August 2025

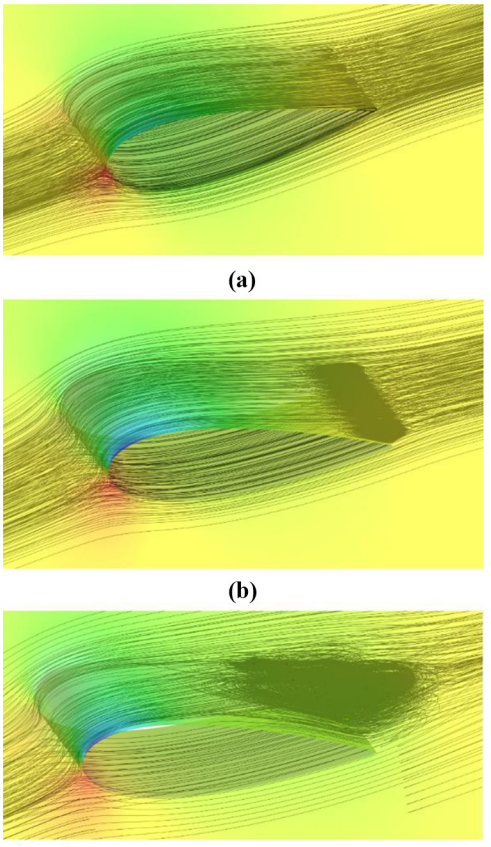

Figure 7.
Streamtraces and pressure coefficient contours at several attack angles for baseline geometry, (a) $\alpha = 5°$, (b) $\alpha = 10°$, (c) $\alpha = 15°$

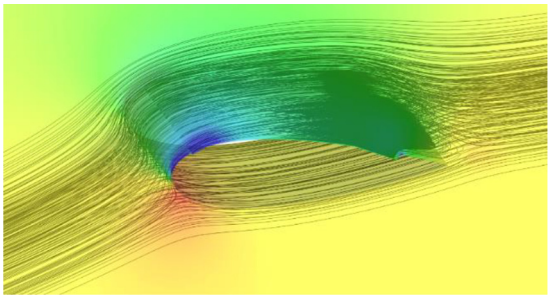

Figure 8.
Streamtraces and pressure coefficient contours for CFJ geometry at $\alpha = 15°$ and $C_\mu = 0.05$

$\alpha = 30°$. Figure 12 shows the stall angles versus the different momentum coefficients. As the momentum coefficient increases, the stall angle increases.

Figure 13 shows the optimum C_μ corresponding to $(C_l/C_d)_{\max}$ for different angles of attack. In other words, each C_μ that leads to maximizing the lift-to-drag ratio is defined as optimum. Within the range of $15° < \alpha < 23°$, by increasing the momentum coefficient, the lift to the drag

Downloaded from http://www.emerald.com/hff/article-pdf/33/6/2278/1441048/hff-04-2022-0219.pdf by Giresun Universitesi user on 17 August 2025

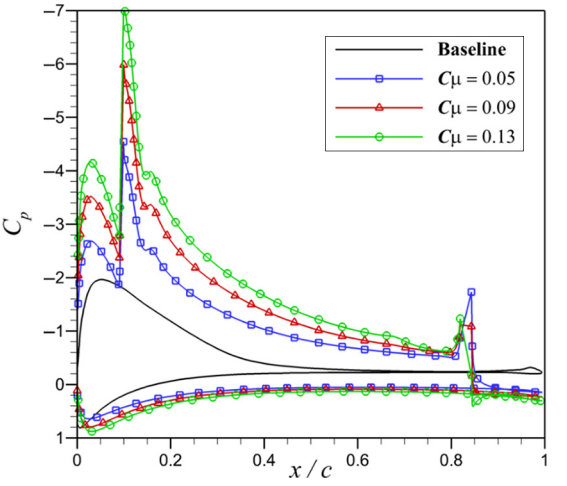

Figure 9.
Comparison of the pressure coefficient distributions at $\alpha = 15°$ for various C_μ levels

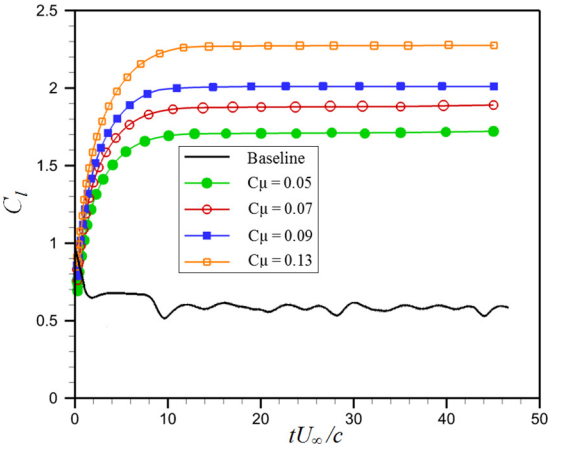

Figure 10.
Temporal variations of lift coefficients at $\alpha = 15°$ for different C_μ levels

ratio is enhanced, increasing the energy consumption of the CFJ. It can also be seen that the CFJ has the highest lift ratio to the drag at 14°. It should be noted that the required momentum coefficient at this angle compared to other angels has the smallest value.

Figure 14(a) and (b) shows the tangential velocity (V_t) profiles for the baseline and CFJ cases with the momentum coefficients $C_\mu = 0.05$ and 0.09 at $x/c = 0.3$ and 0.6, respectively. In both sections, the boundary-layer momentum of the CFJ cases is significantly increased compared to the baseline airfoil.

Table 2 shows the comparison of the maximum lift coefficients and locations of the stall onset between the baseline and CFJ cases. The CFJ significantly increases the maximum lift.

4.4 Effect of coflow-jet on the dynamic stall at re = 1.5 × 10^5

Another investigation in this paper is about the influence of CFJ on the dynamic stall phenomena. The simulation is performed at $k = 0.15$ for the baseline airfoil and two CFJ

Downloaded from http://www.emerald.com/hff/article-pdf/33/6/2278/1441048/hff-04-2022-0219.pdf by Giresun Universitesi user on 17 August 2025

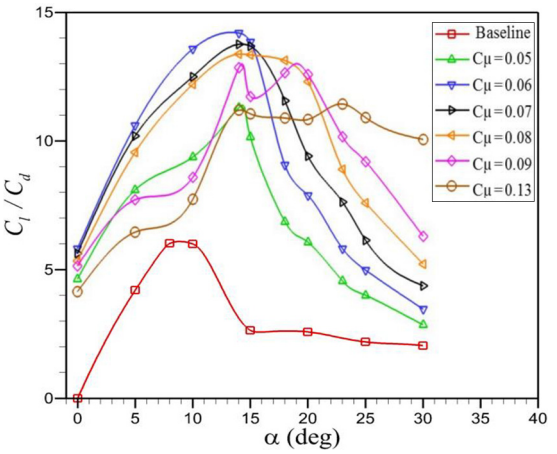

Figure 11.
Comparison of lift to drag coefficients for different C_μ levels

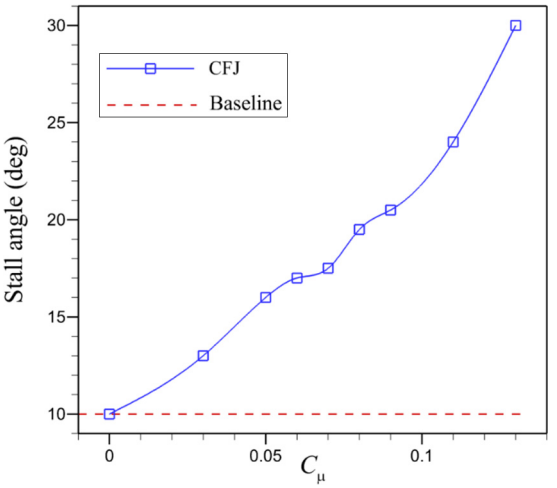

Figure 12.
Variation of stall angles for different C_μ levels

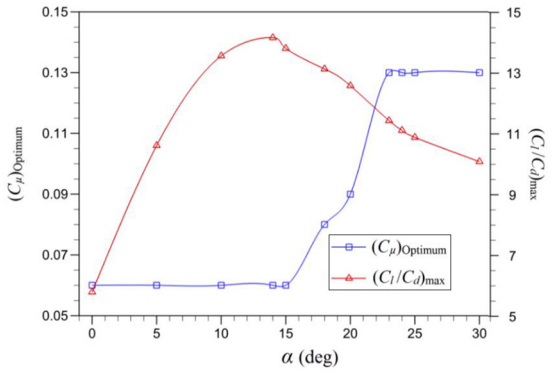

Figure 13.
Optimum C_μ and maximum C_l/C_d for different angles of attack

Downloaded from http://www.emerald.com/hff/article-pdf/33/6/2278/1441048/hff-04-2022-0219.pdf by Giresun Universitesi user on 17 August 2025

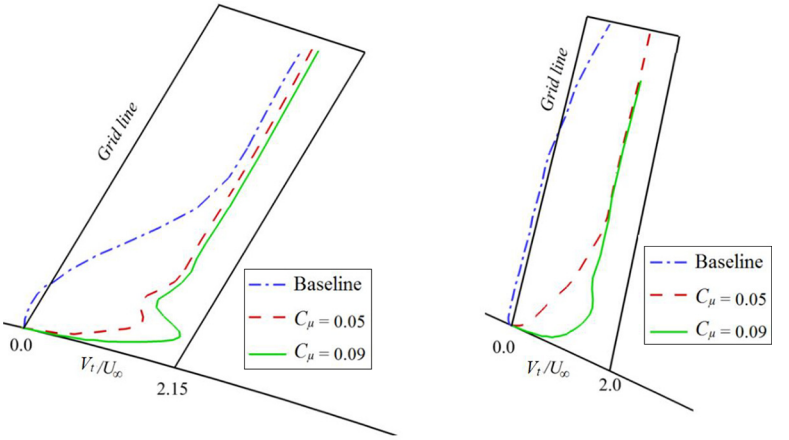

Figure 14.
Comparison of tangential velocity profiles near the airfoil surface at $\alpha = 15°$: (a) $x/c = 0.3$, (b) $x/c = 0.6$

Cases	Maximum C_l	Stall angle (deg.)	Increment in $C_{l\,max}$ relative to the baseline (%)	Increment in stall angle relative to the baseline (deg.)
Baseline	0.6	10	–	–
$C_\mu = 0.05$	1.26	16	110.00	6
$C_\mu = 0.06$	1.76	17	193.33	7
$C_\mu = 0.07$	1.9	17.5	216.67	7.5
$C_\mu = 0.08$	2.16	19.5	260.00	9.5
$C_\mu = 0.09$	2.25	20.5	275.00	10.5
$C_\mu = 0.13$	3.11	30	418.33	20

Table 2.
Comparison of maximum lift coefficients and locations of stall onset

cases with $C_\mu = 0.05$ and 0.07. By increasing the momentum coefficient, more energy can be transferred into the boundary layer; consequently, the lift coefficient is increased. Figure 15 shows the lift coefficient curve for the CFJ control cases and the baseline airfoil. As can be seen, the lift coefficient curve for the CFJ case with $C_\mu = 0.05$ shifts up and is increased, compared to the baseline airfoil; however, the stall still occurs and this behavior is almost similar to the baseline airfoil. As expected, raising the momentum coefficient from 0.05 to 0.07 reduces the lift coefficient hysteresis loop.

Furthermore, in the case of $C_\mu = 0.07$, the lift coefficient curve lacks the stall feature, indicating that a more powerful jet may fully control the dynamic stall. The maximum lift coefficient for the baseline airfoil is equal to 1.15 and for the CFJ cases for $C_\mu = 0.05$ and 0.07 is equivalent to 2.06 and 2.16, respectively. Regarding the drag curves, Figure 16 shows the CFJ control cases with $C_\mu = 0.05$ and 0.07 and the baseline airfoil. The maximum drag coefficient for the baseline airfoil and two CFJ cases is 0.54, 0.32 and 0.21. Therefore, for the case with $C_\mu = 0.07$, the maximum drag coefficient is decreased by 61%; furthermore, its hysteresis loop becomes smaller and smoother.

Table 3 presents the averages of the aerodynamic hysteresis loops for two cases with $C_\mu = 0.05$ and 0.07. To quantify the enhancement in the lift and the reduction in the drag coefficients over a pitch cycle due to CFJ cases, the differences within the area under the C_l

Downloaded from http://www.emerald.com/hff/article-pdf/33/6/2278/1441048/hff-04-2022-0219.pdf by Giresun Universitesi user on 17 August 2025

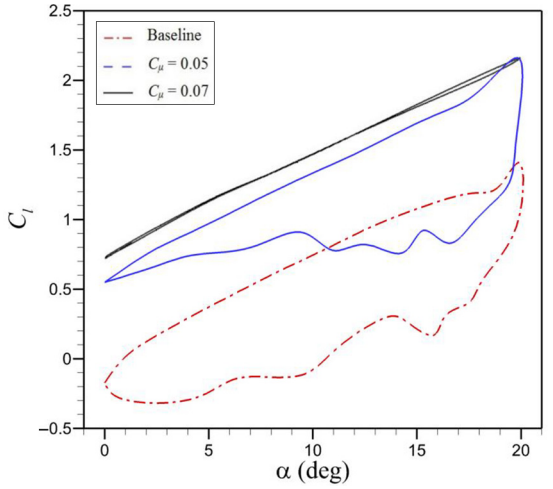

Figure 15.
Lift coefficient comparison between the CFJ and baseline airfoils

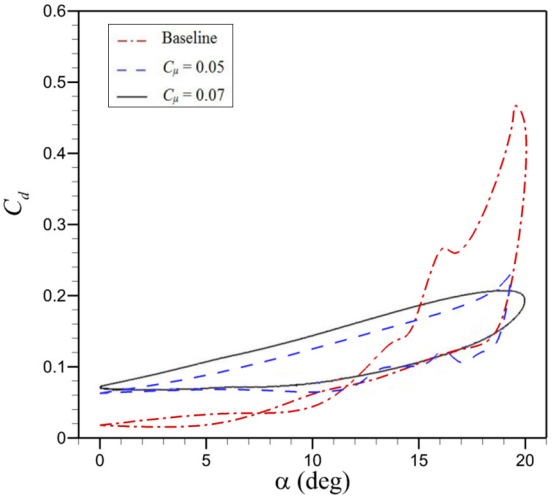

Figure 16.
Drag coefficient comparison between the CFJ and baseline airfoils

Coefficients	Baseline	$C_\mu = 0.05$	$C_\mu = 0.07$
$C_{l,\ ave}$	0.36	1.08	1.44
$C_{d,\ ave}$	0.099	0.11	0.115
$C_{l,\ ave}/C_{d,\ ave}$	3.64	9.82	12.52
ΔA_{C_l}	–	200%↑	300%↑
ΔA_{C_d}	–	12%↑	16%↓

Table 3.
Effects of CFJ control compared to the baseline ($k = 0.15$)

Downloaded from http://www.emerald.com/hff/article-pdf/33/6/2278/1441048/hff-04-2022-0219.pdf by Giresun Universitesi user on 17 August 2025

and C_d curves between the control and baseline cases are computed. The resulting values due to the CFJ control are summarized in Table 3. It is discovered that by adopting the CFJ, the average lift coefficient can be greatly raised and the average drag coefficient can also be somewhat raised. Finally, the results at $C_\mu = 0.07$ show that the relative difference of the lift and drag coefficients $(\Delta A_{C_l}, \Delta A_{C_d})$ are improved compared to the baseline airfoil.

5. Conclusions

The goal of this study is to use numerical analysis to assess the effect of CFJ on the stall and flow separation of the NACA 0024 airfoil at the Reynolds number of 1.5×10^5. The CFJ control used two slots on the airfoil suction surface, one for injection and one for suction. An in-house computer code based on the Reynolds-averaged Navier–Stokes equations, three-dimensional, incompressible and unsteady with the SST k-ω turbulence model, was prepared for this investigation. The solver was verified by comparing it to experimental data, which revealed a reasonably good agreement. In the present study, the performance of CFJ control was evaluated by executing CFJ control at various momentum coefficients and comparing the results to the baseline airfoil. Furthermore, the effects of this flow control on the dynamic stall at two momentum coefficients were studied. The conclusions for $Re = 1.5 \times 10^5$ are as follows:

- The CFJ airfoils compared to the baseline airfoil had a dramatic gain in the lift coefficients and caused the stall to occur at the higher angles of attack maintained with higher values of C_μ.
- Increased momentum coefficients improved the stall angles and maximum lift coefficients of all CFJ airfoils.
- For the angles of attack lower than the stall angles, no improvement was seen by increasing the momentum coefficient compared to the lower momentum coefficients. The trend had almost been stable.
- The baseline airfoil result showed the stall occurring around $\alpha = 10°$, whereas the CFJ airfoil results at $C_\mu = 0.05$ showed the stall occurring at $\alpha = 15°$. With further increase in the momentum coefficients, the stall angles were increased and at $C_\mu = 0.13$, the stall did not happen until $\alpha = 30°$.
- By increasing the momentum coefficient, the drag coefficient increased compared to the baseline airfoil, while for higher angles, increasing the momentum coefficient led to a reduction in the flow separation zone, and consequently, the drag coefficient decreased compared to the baseline airfoil.
- For $\alpha \leq 15°$, C_l/C_d was maximized at $C_\mu = 0.06$.
- The CFJ had the highest ratio of the lift to the drag at $\alpha = 14°$ and $C_\mu = 0.06$.
- In the dynamic stall situation, raising the momentum coefficient from 0.05 to 0.07 resulted in a reduced lift coefficient hysteresis loop. Additionally, with $C_\mu = 0.07$, the lift coefficient curve lacked the stall feature, indicating that a stronger jet could completely manage the dynamic stall.

References

Abbasi, A. and Yazdani, S. (2019), "A numerical investigation of synthetic jet effect on dynamic stall control of oscillating airfoil", *Scientia Iranica*, Vol. 28 No. 1, pp. 343-354.

Abinov, R., Nair, N.R., Sravan, P., Kumar, P. and Nagaraja, S.R. (2016), "CFD analysis of co flow jet airfoil", *Indian Journal of Science and Technology*, Vol. 9 No. 45, pp. 1-5.

Downloaded from http://www.emerald.com/hff/article-pdf/33/6/2278/1441048/hff-04-2022-0219.pdf by Giresun Universitesi user on 17 August 2025

Bak Khoshnevis, A., Yazdani, S. and Salimipour, E. (2020), "Effects of CFJ flow control on aerodynamic performance of symmetric NACA airfoils", *Journal of Turbulence*, Vol. 21 No. 12, pp. 704-721.

Chng, T.L., Rachman, A., Tsai, H.M. and Zha, G.-C. (2009), "Flow control of an airfoil via injection and suction", *Journal of Aircraft*, Vol. 46, pp. 291-300.

Ethiraj, S. (2017), "Aerodynamic performance analysis of a co-flow jet aerofoil using CFD", *International Research Journal of Engineering and Technology*, Vol. 4 No. 7, pp. 987-993.

Ghalambaz, M., Mehryan, S.A.M., Tahmasebi, A. and Hajjar, A. (2020), "Non-Newtonian phase-change heat transfer of nano-enhanced octadecane with mesoporous silica particles in a tilted enclosure using a deformed mesh technique", *Applied Mathematical Modelling*, Vol. 85, pp. 318-337.

Gim, O.-S. and Lee, G.-W. (2013), "Flow characteristics and tip vortex formation around a NACA 0018 foil with anendplate", *Ocean Engineering*, Vol. 60, pp. 28-38.

Gleize, V., Costes, M. and Mary, I. (2022), "Numerical simulation of NACA4412 airfoil in pre-stall conditions", *International Journal of Numerical Methods for Heat and Fluid Flow*, Vol. 32 No. 4, pp. 1375-1397.

Hashem Zadeh, M., Mehryan, S.A.M., Islam, M.S. and Ghalambaz, M. (2020), "Irreversibility analysis of thermally driven flow of a water-based suspension with dispersed nano-sized capsules of phase change material", *International Journal of Heat and Mass Transfer*, Vol. 155, p. 119796.

Kalkote, N., Kumar, A., Assam, A. and Eswaran, V. (2020), "Performance of the k-kL model for aerodynamics applications", *International Journal of Numerical Methods for Heat and Fluid Flow, Vol*, Vol. 22 No. 8, pp. 3985-4011.

Khoshnevis, A., Yazdani, S. and Saimipour, E. (2020), "Analysis of co-flow jet effects on airfoil at moderate Reynolds numbers", *Journal of Theoretical and Applied Mechanics*, Vol. 58, pp. 685-695.

Lee, M., Park, G., Park, C., Kim, C. and Tangchirapat, W. (2020), "Improvement of grid independence test for computational fluid dynamics model of building based on grid resolution", *Advances in Civil Engineering*, Vol. 2020, pp. 1-11.

Lefebvre, A. and Zha, G.-C. (2013), "Numerical simulation of pitching airfoil performance enhancement using co-flow jet flow control", *31st AIAA Applied Aerodynamics Conference*.

Lissaman, P.B.S. (1983), "Low-Reynolds-number airfoils", *Annual Review of Fluid Mechanics*, Vol. 15, pp. 223-239.

Mueller, T.J. and Delaurier, J.D. (2003), "Aerodynamics of small vehicles", *Annual Review of Fluid Mechanics*, Vol. 35, pp. 89-111.

Nived, M.R., Mukesh, B.S., Athkuri, S.S.C. and Eswaran, V. (2022), "On the performance of RANS turbulence models in predicting static stall over airfoils at high Reynolds numbers", *International Journal of Numerical Methods for Heat and Fluid Flow*, Vol. 32 No. 4, pp. 1299-1323.

Rajagopalan, R.G. and Lestari, A.D. (2016), "RK-SIMPLER: explicit time-accurate algorithm for incompressible flows", *AIAA Journal*, Vol. 54, pp. 616-624.

Salimipour, E. (2019a), "A modification of the k-kL-ω turbulence model for simulation of short and long separation bubbles", *Computers and Fluids*, Vol. 181, pp. 67-76.

Salimipour, E. (2019b), "A numerical study on the fluid flow and heat transfer from a horizontal circular cylinder under mixed convection", *International Journal of Heat and Mass Transfer*, Vol. 131, pp. 365-374.

Salimipour, E. and Salimipour, A. (2019), "Power minimization and vortex shedding elimination of a circular cylinder by moving surface mechanism", *Ocean Engineering*, Vol. 189, p. 106408.

Salimipour, E. and Yazdani, S. (2020), "Improvement of aerodynamic performance of an offshore wind turbine blade by moving surface mechanism", *Ocean Engineering*, Vol. 195, p. 106710.

Salimipour, E., Yazdani, S. and Ghalambaz, M. (2021), "Flow field analysis of an elliptical moving belt in transitional flow regime", *The European Physical Journal plus*, Vol. 136, p. 783.

Downloaded from http://www.emerald.com/hff/article-pdf/33/6/2278/1441048/hff-04-2022-0219.pdf by Giresun Universitesi user on 17 August 2025

Saqib Hameed, M. and Kamran Afaq, S. (2013), "Design and analysis of a straight bladed vertical axis wind turbine blade using analytical and numerical techniques", *Ocean Engineering*, Vol. 57, pp. 248-255.

Siddanathi, S.L. (2016), "Application of co-flow jet concept to aircraft lift increase", *International Journal of Advances in Mechanical and Automobile Engineering*, Vol. 3, p. 116206.

Srinath, D.N. and Mittal, S. (2009), "Optimal airfoil shapes for low Reynolds number flows", *International Journal for Numerical Methods in Fluids*, Vol. 61, pp. 355-381.

Stone, H.L. (1968), "Iterative solution of implicit approximations of multidimensional partial differential equations", *SIAM Journal on Numerical Analysis*, Vol. 5, pp. 530-558.

Velasco, D., Lopez Mejia, O. and Lain, S. (2017), "Numerical simulations of active flow control with synthetic jets in a darrieus turbine", *Renewable Energy*, Vol. 113, pp. 129-140.

Wells, A., Conely, C., Carroll, B., Paxton, C. and Zha, G.C. (2006), "Velocity field for an airfoil with co-flow jet flow control", *44th AIAA Aerospace Sciences Meeting and Exhibit*, *Reno, NV*.

Xu, H.Y., Qiao, C.L. and Ye, Z.Y. (2016), "Dynamic stall control on the wind turbine airfoil via a co-flow jet", *Energies*, Vol. 9, p. 429.

Xu, H.Y., Xing, S.L. and Ye, Z.Y. (2015), "Numerical study of the S809 airfoil aerodynamic performance using a co-flow jet active control concept", *Journal of Renewable and Sustainable Energy*, Vol. 7, p. 023131.

Yarusevych, S., Kawall, J.G. and Sullivan, P.E. (2006a), "Airfoil performance at low reynolds numbers in the presence of periodic disturbances", *Journal of Fluids Engineering*, Vol. 128, p. 587.

Yarusevych, S., Sullivan, P.E. and Kawall, J.G. (2006b), "Coherent structures in an airfoil boundary layer and wake at low Reynolds numbers", *Physics of Fluids*, Vol. 18, p. 044101.

Yazdani, S., Salimipour, E., Sheremet, M. and Ghalambaz, M. (2022), "Effects of coflow-jet active flow control on airfoil stall", 04 November 2022, PREPRINT (Version 3) Research Square, doi: 10.21203/rs.3.rs-672095/v3.

Zha, G. and Gao, W. (2006), "Analysis of jet effects on co-flow jet airfoil performance with integrated propulsion system", *44th AIAA Aerospace Sciences Meeting*, *Reno, NV, United States*.

Zha, G., Gao, W. and Paxton, C.D. (2007), "Jet effects on co-flow jet airfoil performance", *AIAA Journal*, Vol. 45, pp. 1222-1231.

Zha, G., Paxton, C., Conley, C.A., Wells, A. and Carroll, B.F. (2006), "Effect of injection slot size on the performance of co-flow jet airfoil", *Journal of Aircraft*, Vol. 43, pp. 987-995.

Corresponding author
Mikhail A. Sheremet can be contacted at: Michael-sher@yandex.ru

For instructions on how to order reprints of this article, please visit our website:
www.emeraldgrouppublishing.com/licensing/reprints.htm
Or contact us for further details: **permissions@emeraldinsight.com**

Downloaded from http://www.emerald.com/hff/article-pdf/33/6/2278/1441048/hff-04-2022-0219.pdf by Giresun Universitesi user on 17 August 2025